Structural Performance Of Cold-Formed Rectangular Hollow Steel Tubular Columns Under Lateral Impact

*Danping Chen, Han Zhou, and Xiaoli Lin

College of Mechanical and Electrical Engineering, Hainan Vocational University of Science and Technology, Haikou 571126, Hainan, China

* *Corresponding author. E-mail: chendanpingok@126.com*

Received Oct. 8, 2025; accepted June 30, 2026

This research provides a numerical evaluation of the impact response of cold-formed rectangular hollow steel tubular (RHST) columns, using finite element models created and validated in ABAQUS/Explicit. A parametric analysis was carried out by varying three major parameters: cross-section properties (wall thickness and section size), impact angles (0°, 45°, and 90°, where 0° corresponds to axial impact, 45° to oblique impact, and 90° to transverse impact orientations), and impact locations (mid-span, L/2, and quarter-span, L/4), while maintaining an approximately consistent global slenderness level across all models. It is observed that the ultimate impact load increases substantially with increasing wall thickness and section size, while thicker, larger sections exhibit better deformation control. Impact orientation also affects the response mode, with 0° and 90° impacts resulting in higher impact loads and global deformations, whereas a 45° impact reduces global response but increases local instability. Impact location also affects impact response, with L/4 impacts generally resulting in higher ultimate impact loads but lower peak displacements than L/2 impacts. Failure modes change from local denting in thin-walled sections to a combination of global buckling and shear deformation in thicker-walled sections. This research can guide designers in designing RHST columns for accidental lateral impact, with consideration of ultimate impact capacity and deformation response.

Keywords: rectangular hollow steel tubes; lateral impact; finite element analysis; dynamic response; ABAQUS simulation.

http://dx.doi.org/10.6180/jase.202611_34.037

1. Introduction

Steel columns are essential structural elements in contemporary buildings, bridges, and infrastructure. Among the various types of steel columns, rectangular hollow steel tubes (RHSTs) offer a cost-effective, lightweight option with an enhanced strength-to-weight ratio compared to the original commercialized steel column [1]. Their resistance to axial, bending, and torsional stresses makes them essential for contemporary construction. They are preferred in specific applications where both strength and aesthetics must be harmonized [2]. The double-tube system of RHSTs is effective for construction and structures that require substantial weight, such as high-rise buildings, offices (industrial structures), and other mega-structures. Nonetheless, akin to all structural components, RHSTs are likely to be affected based on their longevity in relation to the structures themselves [3, 4]. Impact loading of RHSTs can cause substantial damage to the column and the structures it supports, compromising the integrity of its structural performance and ultimately diminishing the component' s functioning [5, 6]. Lateral impact loads pose a significant risk to the design safety assurance of RHSTs; therefore, an in-depth understanding of these columns is essential [7, 8]. Evaluating the impact resistance of RHSTs is crucial to ensuring the safety and durability of any structure exposed to dynamic stresses. Lateral impact loads may result from incidents such as a vehicle colliding with a building or falling debris, potentially causing localized damage, buckling, or even complete failure of the columns if they are inadequately constructed to withstand such forces [9, 10]. The rising demand for larger, more resilient structures in urban settings necessitates assessing and predicting the performance of RHSTs under lateral impact conditions. Understanding lateral impact resistance will ultimately yield design advantages, reduce material consumption, and enhance the safety of building structures.

Many researchers investigated the dynamic behavior and failure modes of laterally hit steel and aluminum tubular columns. Huang and Wang [11] investigate the impact of mid-span penetrating notches on circular hollow steel tubes (CHST) and discover that oblique and horizontal notches significantly enhance indentation and diminish energy absorption, but vertical notches exert less influence. Cui et al. [12] examine lateral impacts on high-strength circular hollow section (CHS) tubes under axial preloading and identify the effects of diameter-to-thickness ratio, impact energy, and axial compression on deformation behavior. Alam et al. [13] investigate full-scale CHS columns reinforced with CFRP subjected to automobile crash loads. CFRP reinforcement was found to be effective in mitigating local buckling and enhancing post-collision residual strength. Korndörfer et al. [14] conducted a series of scaled vehicular impact tests under varying boundary conditions and impact masses, demonstrating that structural interactions lead to significant variations in column damage and in the retention of residual capacity. Li et al. [15] discovered that UHSS hollow tubes subjected to lateral loads exhibited reduced mid-span deflection and improved residual deformation response. Fogarty and El-Tawil [16] contended that lateral loading at column end conditions induces flange buckling, thereby diminishing the axial capacity of steel moment frame columns.

Recent literature has integrated novel materials and pressures. Kerileng et al. [17] examined the performance of duplex stainless steel (DSS) circular hollow section (CHS) tubes subjected to low-velocity lateral impacts. It was shown that when exposed to a laterally applied low-velocity impact, simply supported DSS columns formed a single hinge and largely dissipated energy during the coupling and global deformation phases. The parametric investigation revealed a linear correlation between permanent deformation and impact energy, with negligible influence from cross-section dimensions. Yang et al. [18] performed an experimental and numerical investigation on HSCHS tubes subjected to lateral impact followed by axial compression, resulting in failure characterized by local buckling and global instability. They developed predictive models for the residual axial strength of HSCHS tubes based on critical parameters, including lateral impact energy, slenderness ratio, and compression ratio. Li et al. [19] investigated hollow and foam-filled thin-walled aluminum alloy tubes and observed a significant decrease in structural damage after axial impact with foam filling, especially at higher wall thicknesses. Significantly, impact velocity exerted the greatest influence on both peak force and vertical deflection responses.

Subsequent contributions to the study of lateral impact responses include Zhang et al. [20], who confirmed that local reinforcement enhances impact resistance in stainless-steel tubes; Lipa and Kotełko [21], who analytically modeled the progressive crushing behavior of thin-walled tubes; and Ravaliya and Gupta [22], who reported that tube thickness predominantly dictates energy absorption during the impact of a conical hammer. Dehghanpour et al. [23] examined the comparative behavior under various indenters and cross-sectional forms, revealing that square sections dissipated the maximum energy. Heng et al. [24] introduced a streamlined dynamic model demonstrating plastic hinge behavior and material nonlinearity. Chen et al. [25] presented formulas to predict the residual axial strength of square steel tubes, suggesting a potential drop of around 21% in axial strength upon impact. Siyu et al. [26] illustrated the application of simplified models to evaluate standard columns in steel parking structures subjected to vehicular impacts, revealing straightforward design strategies to prevent collapse of these buildings under such impacts. Yokoya [27] posited that the angle of impact and the axial length will influence the peak loads and deformation modes of polygonal tubes. Moreover, Johnson and Narayanan [28] demonstrated that when a cold-formed stiffened steel tube experiences an eccentric axial stress and is subsequently subjected to a collision with another surface, the reduction in strength is significantly exacerbated. Finally, Fogarty et al. [29] and Segura et al. [30] provided significant insights into failure modes, effective buckling lengths, and boundary restraint conditions, and validated their findings using finite-element and analytical models.

1.1. Research Gap and Novelty

This study examines the lateral impact response of hollow steel sections, recognizing that although significant research has been conducted in this field, most existing work has focused on circular or square hollow sections or on specific impact response features. For columns made from cold-formed RHST, the response in the strong and weak directions, as well as the corners, can give rise to impact responses that are not directly comparable to those of square hollow sections, regardless of geometric similarity. As such, the present investigation offers a unified, validated analysis using ABAQUS/Explicit code, which: considers 16 different RHST geometries based on approximately similar global slenderness, covers three different impact directions (0°, 45°, 90°) and two different impact positions (L/2, L/4), and considers the response in terms of ultimate impact load, maximum displacement, as well as the associated deformation modes, across the entire parametric matrix. Therefore, the purpose of this research is to determine the effect of the cross-sectional shape, impact direction, and impact position on the ultimate impact load, peak deflection, and failure mode of cold-formed RHST columns under lateral impact loading. This study will focus only on hollow RHST columns with predetermined impact energies and end-fixed support conditions. Therefore, the analysis will be limited to the structural behavior trends in this computational model.

2. Numerical investigation

A thorough finite element analysis was conducted to evaluate the lateral impact response of rectangular hollow steel tubular (RHST) columns without concrete filling, in accordance with standard practices used in other implementation studies. The simulated FEA models were analyzed using ABAQUS/Explicit to ensure a precise comprehension of the dynamic behavior and relevant failure mechanisms under various impact circumstances. This section delineates the modeling process, boundary conditions, material specifications, and validation procedure for the RHST columns.

2.1. Finite Element Model Configuration

The geometry of the RHST columns was modeled in ABAQUS using four-node shell elements (S4R), which offer excellent accuracy and computational efficiency for thin-walled structures subjected to significant deformation (Figure 1). The columns incorporated precise modeling of end plates and stiffeners, which were discretized as solid brick elements (C3D8R) to simulate boundary stiffness and load transmission. The pendulum hammer was represented as a stiff analytical surface with a contact area of 200 mm × 50 mm, corresponding to the dimensions of the indenter in the experimental setup [31]. The pendulum hammer was characterized as a discrete rigid body with a specified mass and initial velocity to attain the necessary impact energy for the simulations. The upper and lower plates of the columns were modeled to precisely simulate the restricted conditions.

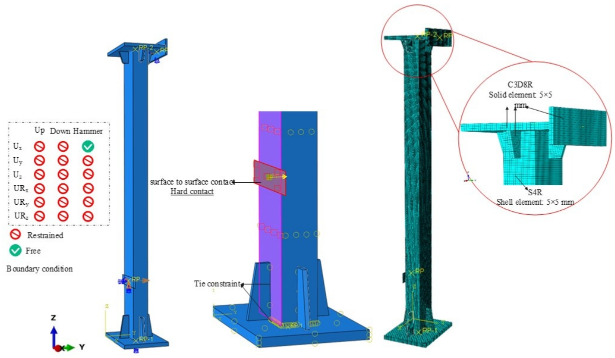

Fig. 1. FEA model of column under lateral impact: boundary conditions, contact interactions, and mesh discretization.

2.2. Mesh Discretization

A mesh sensitivity analysis was conducted to ensure that the numerical results were not significantly affected by the mesh size. Three mesh sizes were considered for the analysis: 2.5 mm, 5 mm, and 10 mm. The 2.5 mm mesh exhibited significant distortion in the impacted zone and terminated early at 7 ms, indicating numerical instability for this mesh size and parameter set. The 5 mm and 10 mm meshes were successfully run, and their displacement-time histories were compared with the experiment (Figure 2). The 5 mm mesh showed better agreement with the experiment for displacement and post-peak behavior, with a peak displacement error of 3.53%. The 10 mm mesh had a larger error of 7.37% (Table 1). Hence, a uniform mesh size of 5 mm x 5 mm is used for all simulations, as it offers a good compromise between accuracy, stability, and computational cost. Stiffness-based hourglass control was used to suppress unwanted deformation modes, and the hourglass energy was kept below 5% of the total internal energy.

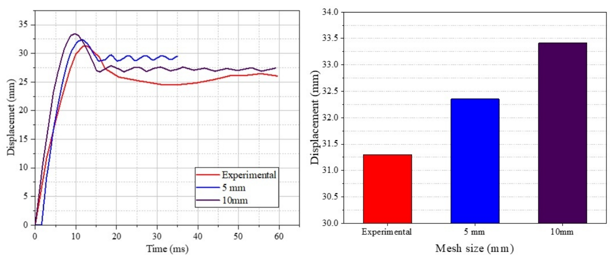

Fig. 2. Mesh sensitivity analysis result.

Table 1. Mesh Sensitivity Results (Peak Displacement Comparison) [31].

Mesh Size	Status	Numerical Peak Displacement (mm)	Experimental Peak (mm)	Error (%)
2.5 mm	Aborted at 7 ms (instability)	–	31.2	–
5 mm	Completed	∼32.3	31.2	∼3–4%
10 mm	Completed	∼33.5	31.2	∼7%

2.3. Material Properties and Constitutive Models

The steel employed for the cold-formed rectangular hollow steel tubular (RHST) columns was modeled using a multi-linear isotropic strain-hardening framework to precisely depict their mechanical behavior under dynamic loading conditions. The model distinguishes between the flat and corner zones of the section to account for strain-hardening effects resulting from the cold-forming process. The material properties for the flat zones were derived using a tensile coupon experiment [31], yielding a yield strength $f_{yn} = 540.6$MPa and an ultimate tensile strength $f_{un} = 616.9$MPa. The modulus of elasticity is defined as E = 2.0 × 105MPa, and Poisson's ratio is given as $v = 0.3$. The corner zones were simulated to exhibit enhanced yield strength due to plastic strain accumulation throughout the forming process. The yield strength (f_{yc}) in the corner zones was calculated using the empirical equation from Abdel-Rahman and Sivakumaran [32] as follows (equation 1):

$$f_{yc} = \left[0.6\left(\frac{r}{t}\right)^{-B} + 0.4\right] f_y \quad (1)$$

Where the parameter B represents material nonlinearity and is defined as equation 2:

$$B = 3.69\left(\frac{f_u}{f_y}\right)^2 - 0.819\left(\frac{f_u}{f_y}\right) - 1.79 \quad (2)$$

This equation represents the local strength enhancement in cold-formed corners, while the equations from Tao et al. [33] are applicable for additional specifics on corner modeling, including the ultimate strength of the corner regions. The Cowper-Symonds strain-rate model [34] was employed to dynamically adjust the yield strength to accommodate high strain rates resulting from lateral impact. The dynamic yield strength f_y^d was calculated using equation 3:

$$f_y^d = \frac{f_y}{1 + \left(\frac{\dot{\varepsilon}}{D}\right)^p} \quad (3)$$

where D $= 40.4^{-1}$ and p $= 5$. This rate-dependent formulation enables the model to precisely depict increases in material strength during rapid loading events, such as impacts, by scaling the yield strength with the strain rate ε°. This comprehensive model accurately represents both the static and dynamic behaviors of cold-formed steel in impact simulations.

2.4. Boundary Conditions and Loading

As seen in Figure 1, the upper and bottom ends of each RHST column were theoretically represented as fixed by constraining all translational and rotational degrees of freedom to emulate a rigid base and replicate test conditions [31]. These limitations ensured that the impact response would be confined to the region of interest, eliminating rigid-body motion from the system. The lateral impact load was applied using a simple pendulum-hammer mechanism, modeled as a discrete rigid body. The hammer operated according to its initial velocity, determined by the potential energy from the pendulum' s release height in the pendulum-release trials [31]. This velocity-dependent approach to impact compelled the simulation to develop the force-displacement relationship throughout the collision. The rigid hammer struck the front or corner of the RHST column, simulating impact energies ranging from 5.82 kJ to 7.46 kJ. This approach enables the indistinguishable replication of brief, high-strain-rate loading conditions encountered in real-world impacts.

2.5. Contact Interactions

The interaction between the rigid hammer and the steel column was specified in ABAQUS utilizing general contact. For the standard orientation, "hard contact" is designated, permitting separation under tensile forces and prohibiting penetration under compressive forces (Figure 1). A Coulomb friction model was employed in the tangential direction, using a friction coefficient of 0.47, as derived by Baltay et al. [35] for steel-to-steel collision under dry conditions.

Table 2. Quantitative comparison between experimental and FE displacement–time responses.

Specimen	Peak disp. EXP (mm) [31]	Peak disp. FE (mm)	Peak displacement error (%)	RMSE (mm)	R^2
H0-C	34.7937	34.0187	2	2.88	0.926
H0-F1	34.3566	35.2	2.5	2.7	0.92

Error (%) = |FE − EXP|/EXP.

2.6. Validation

A validation analysis was conducted to assess the accuracy of the finite element model utilizing both experimental data and published numerical results from Zhu et al. [31]. Two reference specimens, H0-F1 (0° and 90°, 5.13 kJ) and H0-C (45° impact, 2.52 kJ), were selected for their well-documented structural responses and descriptions of failure modes. Figures 3(a) and 3(b) illustrate the impact force–time responses for specimens H0-F1 and H0-C, respectively. The numerical predictions in this work closely mirrored the empirically measured performance during the subsequent behavioral stages: initial peak, vibration decay, plateau, and unloading. The predicted peak forces, impact durations, and plateau shapes were almost identical to the experimental curves. The displacement-time histories for the identical specimens are presented in Figures 3(c) and 3(d). The existing finite element model accurately reproduces displacement histories, matching both the magnitudes and trends of the experimental data. The current FEM accurately captures the increase in displacement rate, rebound behavior, and final values. The quantitative comparison in Table 2 shows good agreement for both validation cases, with R^2 values of 0.926 for H0-C and 0.92 for H0-F1. The peak displacement errors were also limited to 2.0% and 2.5%, respectively, indicating that the FE model can reasonably reproduce the displacement–time response of the tested specimens.

The current finite element has reproduced the local and global deformation behavior observed in studies of failure modes. The finite element model for specimen H0-F1 accurately replicated the local indentation at the impact site, wall buckling, and flexural deformation seen during testing (see Figure 4(a)). The finite element model for specimen H0-C accurately simulated the asymmetric deformation of the affected corner and the localized buckling of each frame (see Figure 4(b)). The local deformation processes closely reflect the actual deformation and experimental data, thereby validating the finite element method's ability to simulate failure localization and overall behavior under lateral impact.

A secondary validation was conducted with reference to the experimental investigation by Zeinoddini et al. [36], which focused on characterizing the impact behavior of steel tubes subjected to an initial axial shortening. In these tests, steel tubes 1000 mm in length were subjected to an initial compressive load and then struck at midspan by a 25.45 kg impactor moving at 7000 mm/s. The above scenarios were also numerically replicated using ABAQUS/Explicit, and the resulting computational assembly is shown in Figure 5. The tube and impactor were modeled using S4R shell elements and C3D8R reduced integration solid elements, respectively, and their material behavior was characterized using an isotropic elastic-plastic material model with an elastic-plastic constitutive relation, which was based on an isotropic formulation of metal plasticity, with material density of 7850 kg/m^3, Young's modulus of 200,000 N/mm^2, yield stress of 500 N/mm^2, and Poisson's ratio of 0.30. The interaction between the striker and the tube was modeled using the general contact algorithm, with hard contact in the normal direction and penalty friction in the tangential direction, along with kinematic constraint enforcement and the small-sliding approximation. The axial pre-compression was applied by specifying a quasi-static step with a reference point, enforcing an axial displacement with a smooth amplitude to avoid spurious dynamic effects. Three specimens, Pd1, Pd2, and Pd3, with different pre-compression levels, were analyzed. As shown in Figure 6, good agreement was observed between the simulated and experimental impact force histories in terms of peak force level, contact time, and the evolution of the transient impact force. Moreover, the post-impact deformation of specimens Pd2 and Pd3 obtained using the proposed method agreed with the experimental ones in terms of local indentation and subsequent global destabilization of the structure, as shown in Figure 7. In conclusion, based on the results of the verification study presented above, the proposed method accurately simulates the impact-time histories and major failure modes of axially pre-compressed steel tubes under transverse impact.

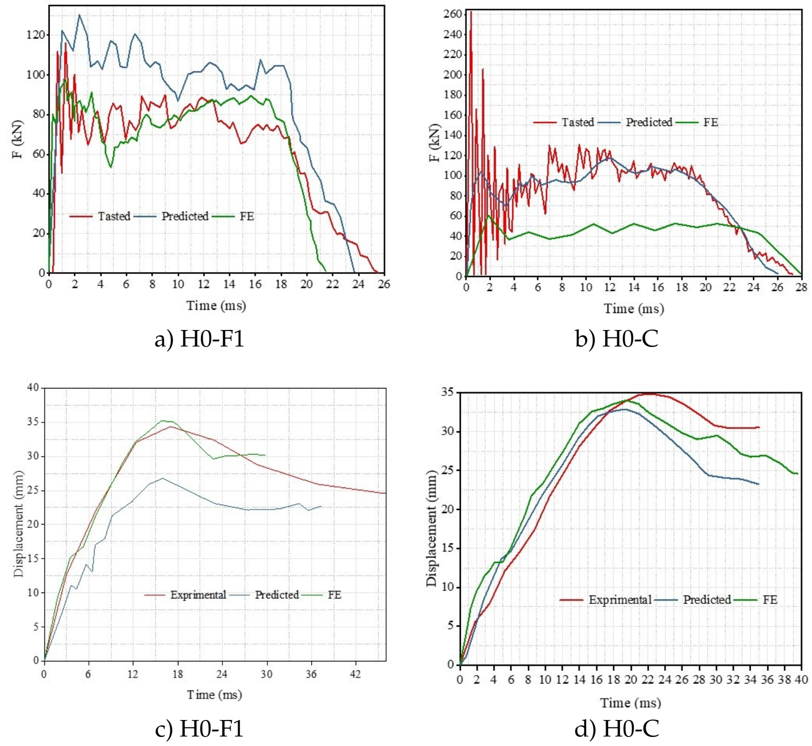

Fig. 3. Impact force–time (F–t) and displacement–time responses of RHST specimens under impact loading [31].

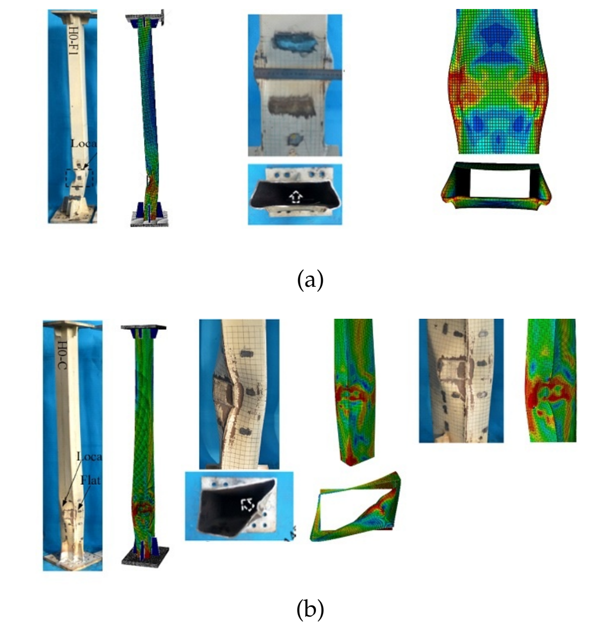

Fig. 4. Comparison of failure modes between experimental and numerical models: (a) specimen subjected to 0° and 90° impact H0-F1; (b) specimen subjected to 45° impact H0-C [31].

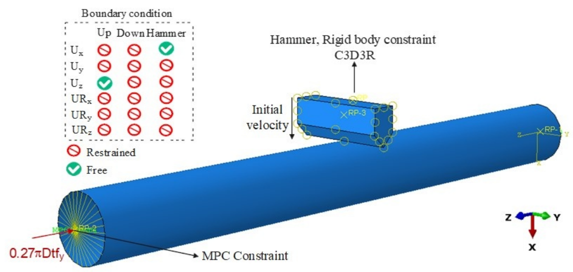

Fig. 5. Finite element model of the validated tube

3. Parametric study

Following the successful validation of FEM, an extensive parametric investigation was conducted to assess the influence of geometry and loading parameters on the lateral impact response of rectangular hollow steel tubular (RHST) columns. The research created 64 finite element models in ABAQUS, based on the verified configuration, to assess structural performance under each designated impact condition. The parametric evaluation required 16 unique rectangular cross-sections created with various combinations of width, height, and wall thickness. Despite variations in the widths and heights of the geometric shapes across different cross-sections, all columns were engineered with

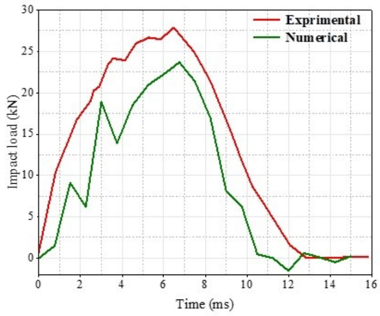

a) Pd1

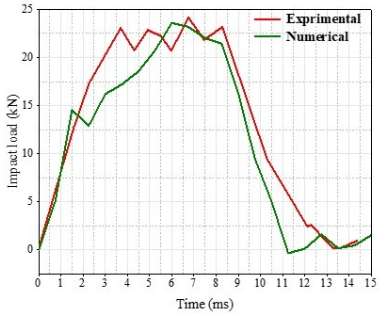

b) Pd2

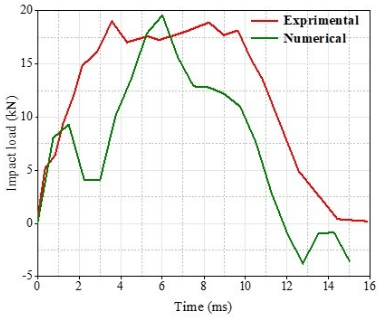

c) Pd3

Fig. 6. Impact force–time responses: experimental measurements versus finite element simulations for the specimens [36].

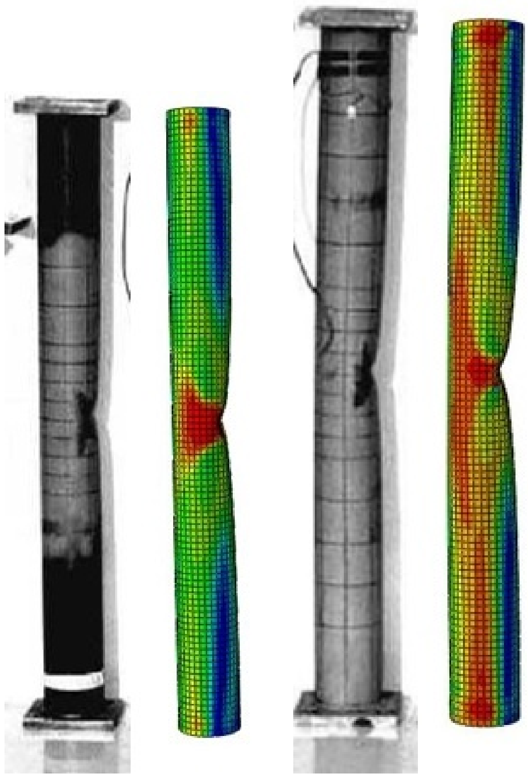

(a) Pd2 (b) Pd3

Fig. 7. Comparison of experimentally observed and numerically simulated failure modes for the specimens [36].

identical slenderness ratios, facilitating a uniform comparison of localized, individual structural reactions within a generally unstable structural framework. The global slenderness ratio has been kept approximately constant for the various parametric models and is defined here as $\lambda = \frac{KL}{r_{\min}}$, where L is the length of the column, K is the effective length factor, and r min is the minimum radius of gyration of the rectangular hollow section about its weak axis. For the fixed-fixed boundary condition considered for the numerical simulation, $K = 0.5$. The sectional properties were calculated using equations 4-7. The calculated values of λ for all cross-sections are given in Figure 8. The crosssections, along with their dimensions used for model formulation, are presented in Figure 8. Two significant effect characteristics were analyzed concurrently with geometric variation. The impact direction was evaluated by applying lateral impact loads at three angles, 0° (axial), 45° (oblique), and 90° (transverse), corresponding to axial, oblique, and transverse impact orientations, respectively. The angles are depicted schematically in Figure 8 and were selected to simulate real-world scenarios, including vehicular collisions and accidental lateral impacts. Secondly, the impact position was evaluated by applying the load at two specific heights of the column, L/4 and L/2, representing one-quarter and one-half of the entire length from the fixed base. These places were selected to examine how structured responses differed as the influence approached boundary limitations. To maintain a common basis for comparison across all cases in this parametric study, a constant impact energy was specified for each group of impact-angle cases. Particularly, a constant impact energy of 5.13 kJ was specified for the 0°, 45°, and 90°impact cases. The impact parameters were consequently set to constant values within this configuration. Table 3 summarizes the impact energy and the corresponding impact velocity adopted for each impact-angle configuration. The decrease in force and displacement characteristics can thus be attributed in part to the lower energy level, although asymmetry and local failure modes are clearly connected to the load direction. To clearly identify each simulation case, a systematic naming procedure was adopted. In this convention, the first symbol denotes the cross-section number (C1, C2, ...), the second term specifies the hammer angle (0, 45, 90), and the final term indicates the impact location (L/4 or L/2). For example, C1-090-L/2 refers to cross-section 1 subjected to a 90° transverse impact applied at mid-height (L/2).

This parametric approach offers a comprehensive analysis of how cross-sectional geometry, impact direction, and impact position influence the dynamic response of RHST columns. The results are expected to yield insights into ultimate impact loads, deformation patterns, and failure mechanisms, ultimately enhancing the design arrangements of steel tube columns in structures exposed to lateral impact hazards.

$$A = BH - (B - 2t)(H - 2t) \tag{4}$$

$$I_x = \frac{BH^3 - (B - 2t)(H - 2t)^3}{12}, \quad I_y = \frac{HB^3 - (H - 2t)(B - 2t)^3}{12} \tag{5}$$

$$r_x = \sqrt{\frac{I_x}{A}}, \quad r_y = \sqrt{\frac{I_y}{A}} \tag{6}$$

$$r_{\min} = \min(r_x, r_y) \tag{7}$$

4. Results

5. The effect of variables on ultimate impact load and displacement under impact loading

The effect of the considered variables on the ultimate impact load and displacement of the RHST columns under lateral impact loading is examined in this section. For better clarity of the comparisons, they are grouped into three parts: cross-Sectional geometries - where each section model (C1-C16) is compared across the considered loading configurations with fixed geometry; impact angle - where comparisons are made across all configurations under each impact angle group of 0° (axial), 45° (oblique), and 90° (transverse); and impact location - where the same model is compared under impact locations of L/2 and L/4. Unless otherwise stated, "variation (%)" refers to the range of values of the considered response quantity from the minimum to the maximum within the considered group of comparisons, calculated as in equation 8, where X denotes the ultimate impact load or peak displacement. These comparisons are then assessed against three response measures: ultimate impact load, peak displacement, and actual deformation/failure behavior. In other words, performance is considered as the ability of the proposed RHST columns to resist higher impact loads, control displacement, and prevent or change the onset of instability in the investigated models. It must be stressed that the performance measure presented here is not an indicator of the whole structure's integrity and post-impact strength.

$$\mathit{Variation}\ (\%) = \frac{(X_{\max} - X_{\min})}{X_{\min}} \times 100 \tag{8}$$

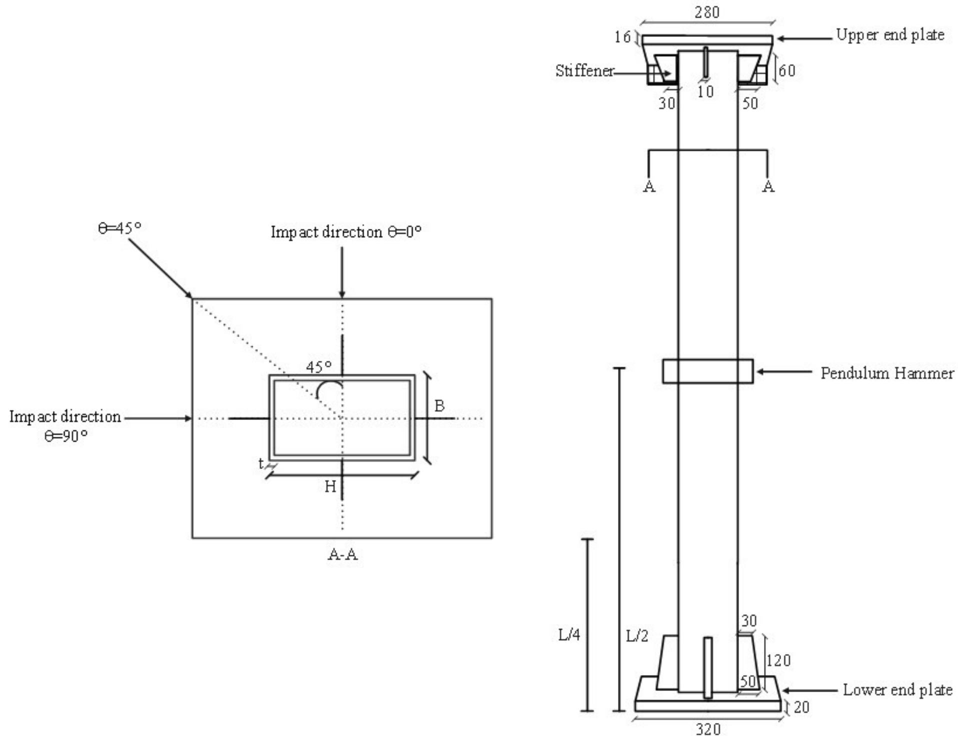

Model	t (mm)	B (mm)	H (mm)	L (mm)	r_{min} (mm)	$\lambda = KL/r_{\min}$
C1	2	80	110	3383	33.11	51.08
C2	2	80	120	3653	33.44	54.62
C3	2	90	130	3983	37.56	53.02
C4	2	100	140	4312	41.68	51.73
C5	3	80	110	3351	32.71	51.22
C6	3	80	120	3620	33.04	54.79
C7	3	90	130	3951	37.16	53.16
C8	3	100	140	4280	41.27	51.85
C9	4	80	110	3319	32.32	51.35
C10	4	80	120	3588	32.64	54.96
C11	4	90	130	3919	36.76	53.30
C12	4	100	140	4248	40.88	51.96
C13	5	80	110	3288	31.93	51.49
C14	5	80	120	3557	32.25	55.15
C15	5	90	130	3887	36.37	53.44
C16	5	100	140	4216	40.48	52.07

Fig. 8. Geometric and loading specifications of FEA parametric models.

Table 3. Impact loading parameters adopted in the parametric study.

Impact configuration	Impact angle (°)	Impactor mass, m (kg)	Velocity components (mm/s)	Impact velocity, v (mm/s)	Impact energy, E (kJ)
Front impact	0	243	6500	6500	5.13
Corner impact	45	243	$v_x = v_y = 4596.2$	6500	5.13
Front impact	90	243	6500	6500	5.13

$$E = 0.5mv^2 = mgh$$

6. Cross-sectional geometries

The cross-sectional models C1 to C16 offer significant comparative data on hollow rectangular steel columns exposed to lateral impact loading, encompassing the influences of wall thickness (t = 2 to 5 mm), width (B = 80 to 100 mm), height (H = 110 to 140 mm), and length (L = 3288 to 4312 mm), while preserving a uniform slenderness ratio. The regulated methodology ensured that only the cross-sectional dimensions influenced the final impact load and peak displacement, facilitating direct performance evaluation of cross-sectional designs. The load-time and displacement-time histories for these columns are illustrated in Figure 9a, while Figure 9b presents the correlation between cross-sectional geometry and structural performance.

It is important to note that the increase in ultimate impact load with increasing wall thickness and cross-sectional size is explained by increases in sectional stiffness, moment of inertia, section modulus, and local plate stability. In thin-walled members, there was insufficient out-of-plane stiffness on the impacted side; therefore, the impact load was concentrated over a small area, leading to premature local denting, bending of the web or flanges, and localized buckling of the impacted member. It explains the large scatter in the ultimate impact load and peak displacement for samples with a 2 mm wall thickness due to sensitivity to changes in impact angles and locations. With the increase in wall thickness from 2 mm to 5 mm, the slenderness of the plate elements decreased, making them less prone to local buckling and, therefore, allowing more distribution of impact forces over a cross-section. Larger sections exhibited greater resistance to plastic deformation and could withstand higher impact loads. The numerical results confirm this, showing that the maximum ultimate impact load for the largest section (5 mm wall thickness) is 149.72 kN.

7. The angle of the impactor

This investigation examined the role of impact orientation using hammer angles of 0° (axial), 45° (oblique), and 90° (transverse). Impact energy was set to 5.13 kJ in all 0°, 45°, and 90° cases. The mode of deformation experienced in the 45° cases, which includes asymmetric local instability and torsional-flexural coupling, indicates the unique effect of oblique load orientations. The effect of the angle of impact could also be explained by changes in the load path and deformation mode. Impact angles of 0° and 90° correspond to an impact load applied along one of the primary bending planes of the rectangular hollow cross-section. As a result, deformation is controlled by the section's flexural stiffness in the particular plane, together with the localized indenter response to the impact. In the case of 45° orientation, bending in two perpendicular planes and torsion around the longitudinal axis of the column are involved. It reduces the effectiveness of the load path and promotes asymmetric deformation, corner instabilities, and twisting in the impacted area. Therefore, 45° impact specimens have lower impact resistance compared to 0° and 90° impact specimens. However, local corner instability and twisting are more pronounced for the 45° impact samples. Hence, the differences among the three modes of impact are not merely quantitative but involve distinct mechanisms and regimes of deformation. The 45° cases showed lower impact force and displacement; however, this reduction should be interpreted with caution, as these cases were simulated with lower impact energy than the 0° and 90° cases. Therefore, the lower global response cannot be attributed solely to the impact angle. The main effect more directly associated with the oblique impact orientation is a change in the deformation mechanism, including asymmetric buckling, local instability, and combined torsional-flexural deformation.

8. Impact location

The examination of impact sites on hollow rectangular steel columns provides significant insights into how load positioning affects the final impact load and maximum displacement. This study selected two places for impact: mid-span (L/2) and quarter-span (L/4), which are critical in structural design due to the varying forces and moments that emerge at each position along the column' s length. The findings are visualized in Figure 11a, which presents the time-history analysis of impact load and displacement for different impact locations, and in Figure 11b, which outlines the structural response associated with each impact site.

The influence of impact location is determined by interactions of bending moment distribution, effective length of deformation, and boundary conditions. At impact point L/2, an increased effective bending length of the column, along with a symmetric global deformation mode, leads to higher lateral displacement due to increased distance from the rotational boundary condition caused by the fixed supports. In contrast, when impact is applied at L/4, proximity to the fixed boundary makes the local boundary condition stronger while reducing the effective deformation length. As a result, maximum displacement decreases, whereas the apparent resistance to impact increases. That explains why ultimate impact loads were higher for L/4 than for L/2 impacts, while peak displacements were smaller for the former case. For example, the ultimate impact force increased

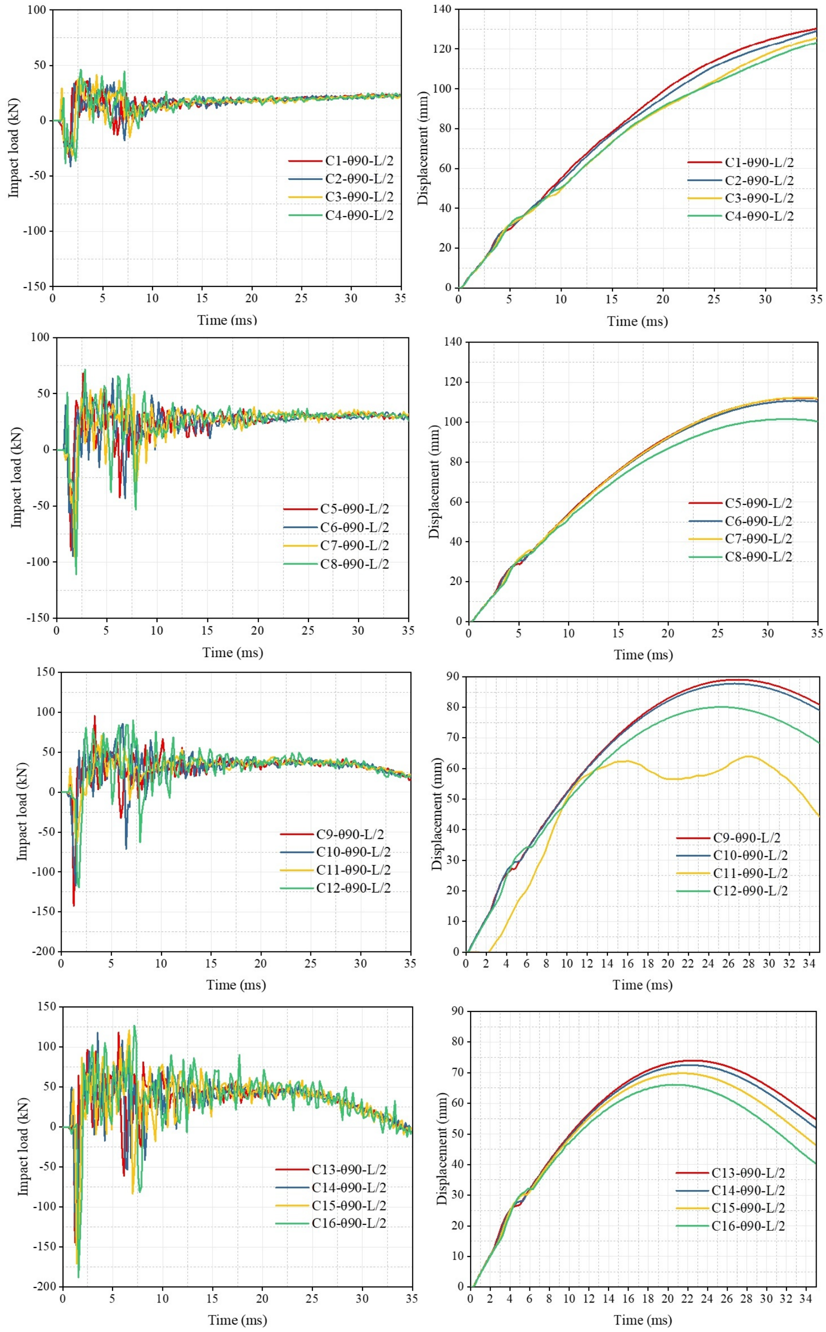

(a) Time-history analysis of impact load and displacement for RHST columns with different cross-sections

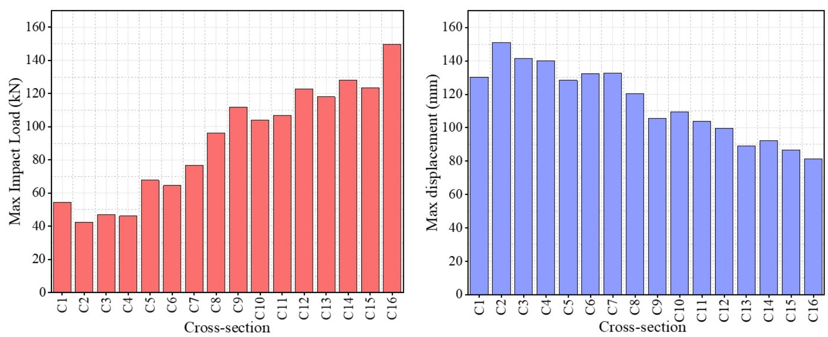

(b) Relationship between cross-section geometry and structural response under impact.

Fig. 9. Dynamic response analysis of RHST columns with different cross-sections under impact loading.

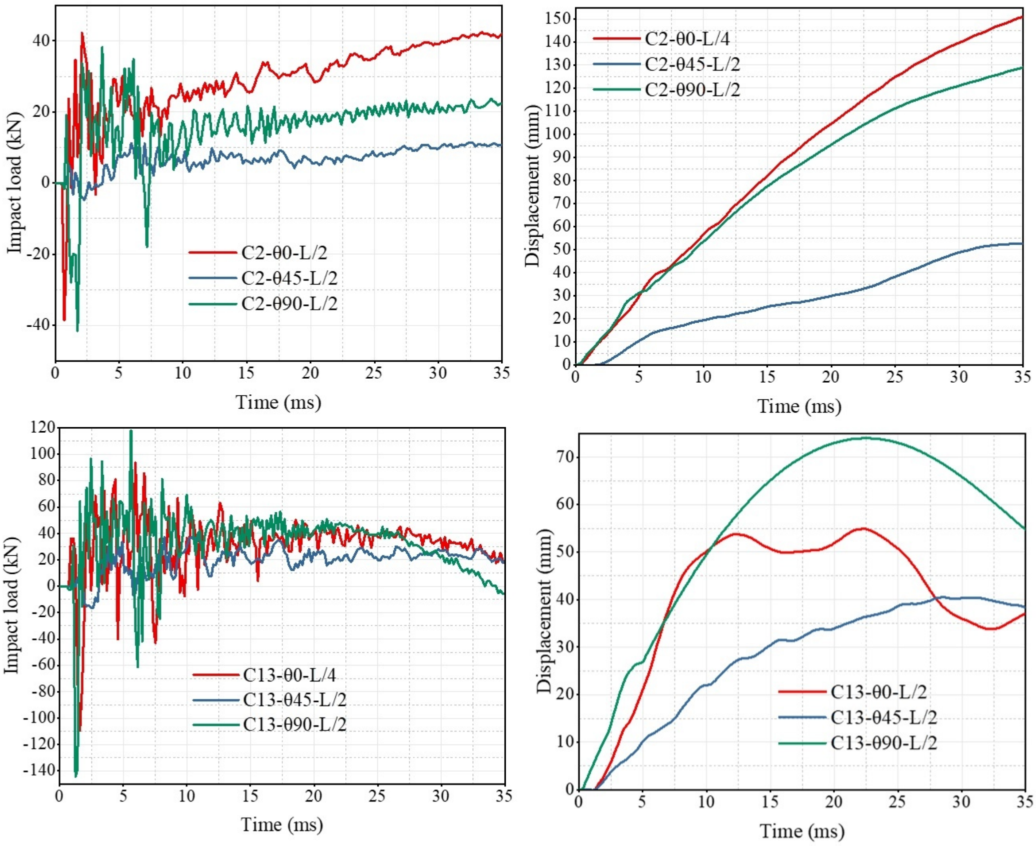

(a)

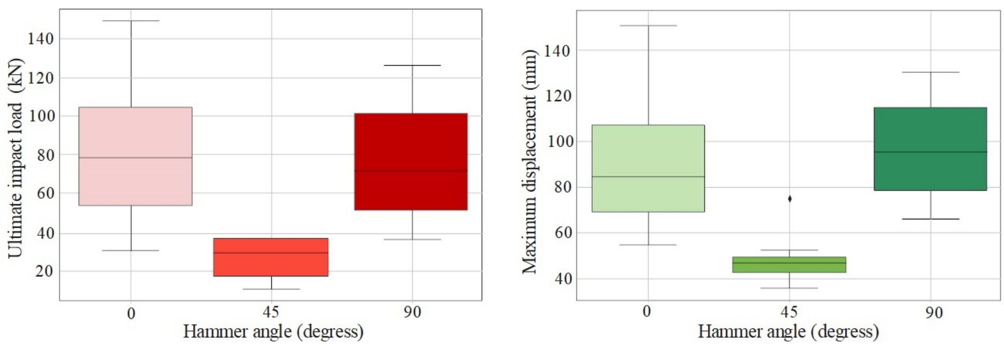

(b)

Fig. 10. a) Time-history analysis of impact load and displacement for RHST columns with different impact angles; b) Relationship between impact angle and structural response under impact.

from 105.48 kN for the L/2 impact location to 149.72 kN for the L/4 impact location, which was an increase of about 42% for the highest section. Nevertheless, such high-impact load capacity came at the cost of the shear-torsional mode of deformation. Thus, L/4 impact cannot be treated as significantly less critical than the L/2 case as it just indicates a difference in mechanisms of failure – with the former requiring higher force and less displacement.

9. Failure mode analysis and discussion

The performance of cold-formed steel columns is predominantly influenced by their cross-sectional geometry, including wall thickness and overall dimensions. As demonstrated in Figure 12a, the thin-walled sections (e.g., models C1 to C4, with wall thicknesses of 2 mm) exhibited a heightened tendency for localized failure modes. The thin-walled parts primarily failed due to localized denting, local bending of the web and flanges, and in certain models, material failure occurred at the point of contact. The structural stiffness and energy-dissipation capacities of the thin-walled sections are dramatically reduced, and the failure modes commence considerably earlier in the deformed impact state, as evidenced by the substantial post-impact deformations. When increasing the wall thickness from 3 mm to 4 mm (e.g., from models C5 to C12), a shift in failure mechanisms was observed from localized, concentrated impacts to a more dispersed reaction. The medium-thickness sections exhibited a combination of local and global failure modes. Local buckling persisted but was integrated with the flexural deformation of the entire member. The augmented cross-sectional area enhanced resistance to starting denting and postponed the overall onset of instability. The mechanisms of distributed plasticity were notably consistent, with plastic hinge formation occurring farther from the impact site. In the most resistant column group (C13 to C16, with a 5 mm wall thickness), the failure modes exhibited more extensive deformation, including shear buckling, flexural-torsional deformation, and, in some instances, significant plastic hinge development without significant local tearing. The thicker parts exhibited a notable increase in impact resistance, absorbing greater energy until failure while maintaining structural integrity for extended periods. The augmented moment of inertia and section modulus in these models enhanced their resistance to both local indentation and global collapse mechanisms.

The hammer angle at impact significantly influences the angles, magnitudes, and distributions of stresses, thereby affecting the failure modes of the columns. As illustrated in Figure 12b, when impact was administered in the horizontal plane ($\theta = 0°$), the column exhibited a greater in-plane flexural response. The deformation was primarily symmetrical, with plastic hinges developing in the impact zone, as anticipated, and frequently (though not uniformly) around the mid-span, predominantly in the in-plane direction. Global bending moments caused this failure, characterized by lateral displacement along its length and predominantly localized damage at the impact site. At $\theta = 45°$, the failure mode and overall behavior of the columns were ambiguous. As the angle grew to $\theta = 45°$, the intermediate oblique loading placed the column between an underloaded state and the out-of-plane failure mode. The new loading scenario introduced an oblique force component along with the in-plane loading components, resulting in greater column twisting at the impact site. Furthermore, the twisting and buckling failure of the columns led to asymmetric buckling, deviating from the typical symmetrical buckling observed at $\theta = 0°$. Additionally, columns of intermediate thickness exhibited local instabilities alongside the global reaction, leading to a partially twisted combined failure mode characterized by bending, torsion, and localized yielding. The most substantial damage occurred under vertical impact conditions ($\theta = 90°$). This scenario resulted in very localized and severe pressures at the contact point, causing considerable denting and localized yielding or tearing, particularly in the thinner-walled columns. The deformation was highly limited, and the failure transpired without considerable global displacement. In the thicker areas, despite localized damage, the enhanced stiffness inhibited penetration and facilitated stress redistribution, resulting in shear-dominated failure modes.

Figure 12c demonstrates that the position of the applied load (mid-span L/2 or quarter-span L/4) significantly influences the mode of failure due to its impact on internal forces and boundary conditions. At mid-height (L/2), these columns typically failed symmetrically due to global flexural buckling, accompanied by plastic hinging in the impact region. The resultant significant deformation and curvature were predominantly concentrated at the center of the column, which endured the greatest load (striking, bending) and coincided with the location of the natural global maximum bending moment under such loading conditions. In contrast to the mid-height loadings, the column exhibited asymmetric loading and deformation when the impact was applied at L/4, attributable to the eccentric application. The outcome of the eccentric loading was moment-arm asymmetry and a preferential stress concentration at or near the supporting fixed end, resulting in a more complex failure mode, including lateral-torsional buckling, secondary plastic hinges near the fixed end, and increased susceptibility to shear deformation compared to flexural deformation.

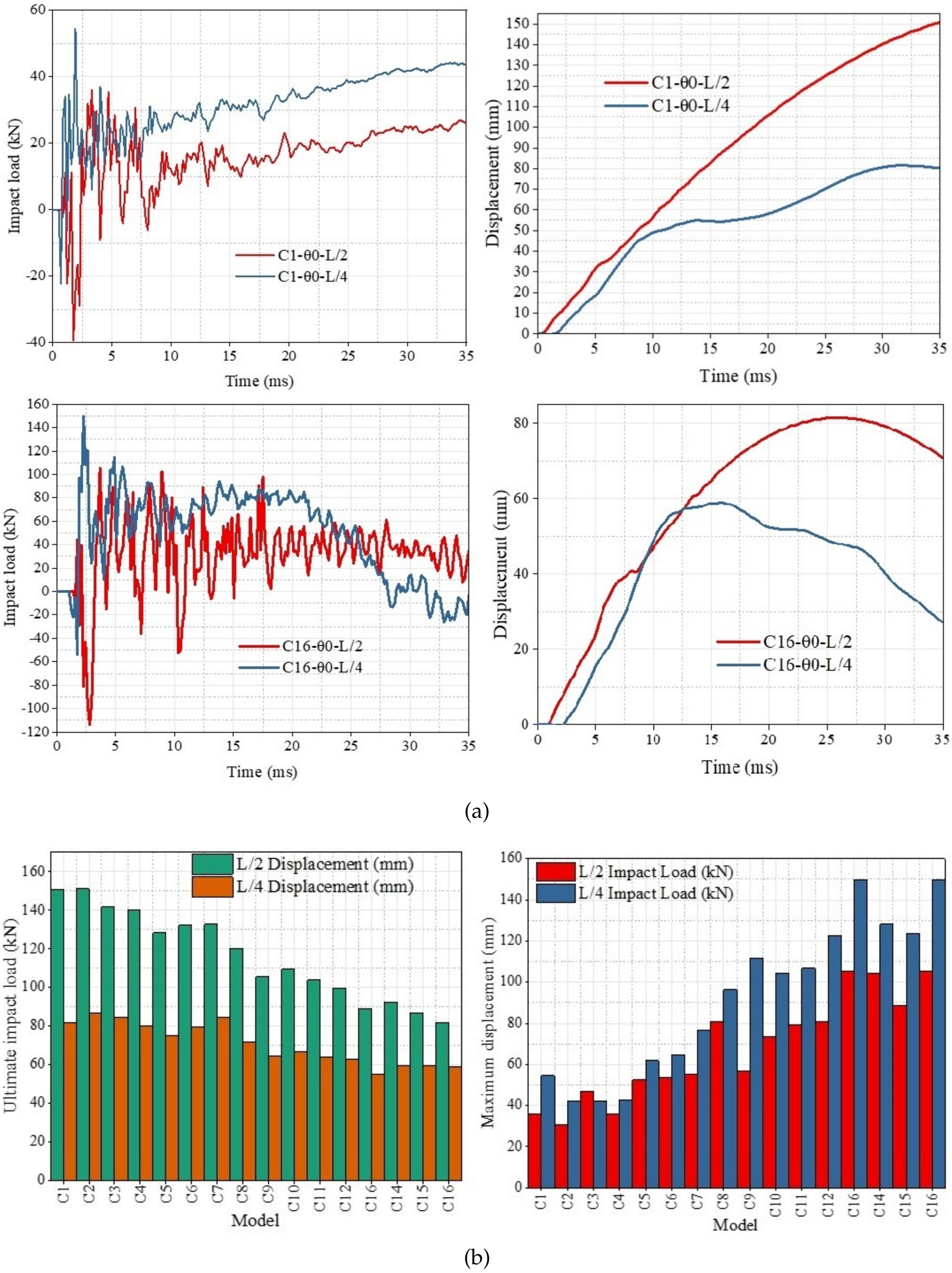

Fig. 11. a) Time-history analysis of impact load and displacement for RHST columns with different impact locations; b) Relationship between impact location and structural response under impact.

The local deformation response of the thin-walled columns was more pronounced due to loading constraints near the supports, resulting in a reduction in lateral resistance. The thick-walled column exhibited predominant torsional and shear-dominated deformations, with minimal global flexural bending. The results mentioned above highlighted the susceptibility of cold-formed steel columns to the impact location, particularly with respect to symmetry, moment distribution, and failure propagation. The structure' s capacity to resist collapse is significantly dependent on the interaction between loading position and boundary conditions.

9.1. Conclusion

This study conducted a substantial numerical analysis of the lateral impact behavior of cold-formed rectangular hollow steel tubular (RHST) columns, using finite element modeling in ABAQUS/Explicit, and validated it through experimental testing. The research comprised a design study that assessed three primary parameters: cross-sectional geometry, impact angle, and impact location. Furthermore, all variations exhibited a consistent slenderness ratio throughout the modeled testing. The findings provided insights into the structural response and failure criteria of RHST columns under dynamic lateral loading. The research indicates that the thickened walls related to cross-sectional geometry, particularly wall thickness and sectional depth, are the most critical factors influencing impact resistance in RHST columns. The thicker-walled, larger-section columns produced higher final impact loads and lower displacements than the thinner-walled columns. The ultimate impact load increased by over 100% when the wall thickness was increased from 2 mm to 5 mm, with model C16 achieving the highest recorded value of 149.72 kN. The failure modes evolved, with local denting and premature buckling in the thinner wall sections transitioning to more global deformation and plastic hinges in the thicker wall sections and larger cross-sections, thereby enhancing structural integrity under lateral impact conditions. The angle of impact significantly influenced load absorption and failure mechanisms. At 0° impact, the highest peak loads were generated but also led to increased displacements and significant flexural damage, indicating ductile behavior. A 90° lateral impact resulted in more concentrated and localized damage, particularly characterized by indentation in thin-walled parts. Oblique impacts at 45° resulted in more intricate torsional-flexural failure modes, particularly in the intermediate portions. These findings indicate that angular vulnerability must be incorporated into design evaluations, since variations in impact may alter the trajectory of failure propagation. The impact location was determined to significantly influence the dynamic response. Impacts applied at mid-height (L/2) led to increased displacements and reduced impact resistance because the imposed load increased moment demands. A quarter-span (L/4) moment or load exhibited enhanced structural performance owing to significantly reduced loads. Specimens affected at L/4 exhibited ultimate loads that were 42% higher than those of mid-span-impacted specimens with the identical cross-section (i.e., model C16). The failure mechanism for L/4 was driven by torsion and shear, whereas the mid-span failure exhibited symmetric global buckling due to reduced moment demands. The location of the anticipated impact significantly influences two primary aspects: 1) the structural performance limits of the member and 2) the deformation pattern. The research indicates that increased wall thickness and cross-sectional dimensions must be considered in the design of RHST columns to accommodate side impact. The design permitted enhanced dimensions at critical points of resistance and would have been improved by eliminating thin-walled columns in the susceptible mid-span areas. A thorough assessment reveals that members with thin walls and no reinforcement significantly affect the design, particularly at points of impact. Similar considerations apply to angular effects that may result from perceived collisions with protective design, in which different angles influence distinct types of instability and deformation. As with other studies, this study has inherent limitations. These limitations pertain to its application to hollow RHST columns, which do not experience axial stresses, and to the complications introduced by concrete infill on other boundary conditions or restrictions. The study' s limitations are also predicated on the low impact velocities. In any practical scenario, the elements represented in the study for impact, along with the modeling presented in this paper, could illustrate damage characteristics such as strain-rate-dependent effects, connection effects, and catastrophes or material imperfections. Subsequent studies should include concrete-filled tubular sections, axial loading, and various support conditions to enhance the realism of the scenarios examined. Experimental testing at elevated strain rates and probabilistic modeling of impact-related uncertainties would enhance safety margins and establish generalized design guidelines. Future research may investigate hybrid reinforcement techniques or examine energy-dissipation mechanisms. This method would offer novel opportunities to enhance the structural robustness of steel columns in critical infrastructure.

The conclusions drawn from this study are limited to the investigated cold-formed hollow RHST columns, impact-

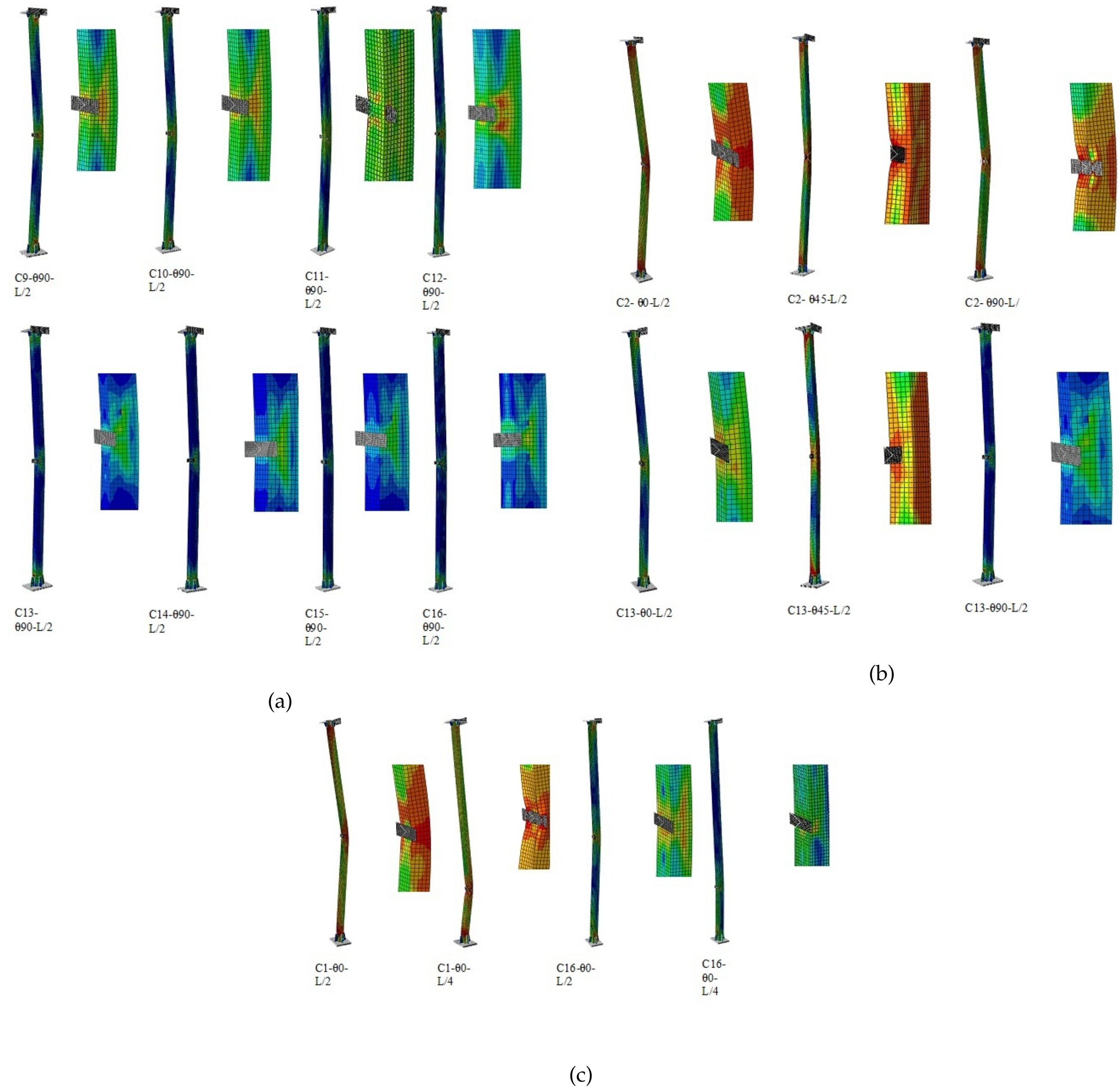

Fig. 12. Influence of a) cross-section geometry, b) impact angle, and c) impact location on failure modes of RHST columns.

energy levels, impact orientations, impact locations, and fixed-end boundary conditions. Within this scope, thicker and larger sections yielded higher ultimate impact loads and lower peak displacements, while impact orientation and location altered the governing deformation modes. These findings provide useful numerical insight into lateral impact response, but they do not constitute generalized design provisions. Future studies should include experimental verification over a wider parameter range, axial load effects, concrete-filled or strengthened sections, different support conditions, and residual-capacity assessment after impact.

Funding

This work was supported by the Education Department of Hainan Province under project number Hnky2022ZD-20.

nomenclature

Acronyms	
ABAQUS	A software suite for finite element analysis
C3D8R	8-node linear brick element with reduced integration
CHS	Circular Hollow Section
EAbs	Energy Absorbed
FE / FEA	Finite Element / Finite Element Analysis
GBT	Global Buckling Threshold
L/2	Mid-height impact location (half of the total column length)
L/4	Quarter-height impact location (one-fourth of total column length)
PD	Peak Displacement
PRC	Plastic Resistance Capacity
RHST	Rectangular Hollow Steel Tubular
S4R	4-node doubly curved shell element with reduced integration
UIL	Ultimate Impact Load
Greek Symbols	
$\dot{\varepsilon}$	Strain rate (s^{-1})
σ_d	Dynamic yield stress (MPa)
Θ	Impact angle ($0°, 45°, 90°$)
Superscripts	
B	Width of the column cross-section (mm)
B (in equation)	Material nonlinearity parameter
D	Cowper–Symonds strain rate constant (40.4)
E	Young's modulus of steel (MPa)
F	Impact force (N or kN)
f_{un}	Ultimate tensile strength of flat zone (MPa)
f_{yc}	Yield strength of corner zone (MPa)
f_{yn}	Yield strength of flat zone (MPa)
H	Height (or depth) of the column cross-section (mm)
L	Length of the column (mm)
N	Poisson's ratio
P	Cowper–Symonds strain rate exponent (5)
T	Wall thickness of the column (mm)
t (in F–t)	Time (s)
U	Displacement (mm)

References

[1] A. Poursadrollah, M. D'Aniello, and R. Landolfo, (2022) *"Experimental and numerical tests of cold-formed square and rectangular hollow columns"* **Engineering Structures** ***273***: 115095. DOI: https://doi.org/10.1016/j.engstruct.2022.115095.

[2] P. Ayough, Z. Ibrahim, N. H. R. Sulong, and P.-C. Hsiao, (2021) *"The effects of cross-sectional shapes on the axial performance of concrete-filled steel tube columns"* **Journal of Constructional Steel Research** ***176***: 106424. DOI: https://doi.org/10.1016/j.jcsr.2020.106424.

[3] R. B. Tank, V. B. Patel, I. N. Patel, and D. R. Bhatt, (2025) *"Comparative Study of Bundled Tube System with Bracing System for High Rise Building"* **International Advanced Research Journal in Science, Engineering and Technology (IARJSET)** ***12***: 200–210. DOI: 10.17148/IARJSET.2025.12123.

[4] X. Chen, S. Li, Z. Yu, J. Xu, L. Wang, Y. Pei, W. Zhang, Z. Jing, L. Min, and Y. Wang. "Application of Key Technologies for Multi-Terminal Change of Frame-Double Core Tube Super High-Rise Building". In: *IOP Conference Series: Earth and Environmental Science*. ***692***. IOP Publishing, 2021, 022090. DOI: 10.1088/1755-1315/692/2/022090.

[5] W.-D. Wang, L. Zheng, and W. Xian, (2022) *"Performance of the CFST column to composite beam connection under static and impact loads"* **Journal of Constructional Steel Research** ***198***: 107567. DOI: https://doi.org/10.1016/j.jcsr.2022.107567.

[6] C. Demartino, J. Wu, and Y. Xiao, (2017) *"Experimental and numerical study on the behavior of circular RC columns under impact loading"* **Procedia Engineering** ***199***: 2457–2462. DOI: https://doi.org/10.1016/j.proeng.2017.09.386.

[7] W. Zhao and J. Ye, (2022) *"Dynamic behavior and damage assessment of RC columns subjected to lateral soft impact"* **Engineering Structures** ***251***: 113476. DOI: https://doi.org/10.1016/j.engstruct.2021.113476.

[8] L. Kang, W. Fan, B. Liu, and Y. Liu, (2021) *"Numerically efficient analysis of concrete-filled steel tubular columns under lateral impact loading"* **Journal of Constructional Steel Research** ***179***: 106564. DOI: https://doi.org/10.1016/j.jcsr.2021.106564.

[9] A. Chen, Y. Liu, R. Ma, and X. Zhou, (2023) *"Experimental and Numerical Analysis of Reinforced Concrete Columns under Lateral Impact Loading"* **Buildings** ***13***: 708. DOI: https://doi.org/10.3390/buildings13030708.

[10] D. Yating. "Research on Lateral Impact Resistance of Concrete Filled Steel Tubular Columns". In: *2022 12th International Conference on Information Technology in Medicine and Education (ITME)*. IEEE, 2022, 766–769. DOI: https://doi.org/10.1109/ITME56794.2022.00160.

[11] X. Huang and Y. Wang, (2023) *"Lateral impact response of circular hollow steel tubes with mid-span localized penetrating notches"* **Frontiers in Materials *10***: 1321892. DOI: https://doi.org/10.3389/fmats.2023.1321892.

[12] G. Cui, X. Zhai, and L. Meng, (2023) *"Behavior of axially loaded high-strength steel circular hollow section tubes under low velocity lateral impact"* **Thin-Walled Structures *185***: 110595. DOI: https://doi.org/10.1016/j.tws.2023.110595.

[13] M. I. Alam, S. Fawzia, X.-L. Zhao, and A. M. Remennikov, (2020) *"Numerical modeling and performance assessment of FRP-strengthened full-scale circular-hollow-section steel columns subjected to vehicle collisions"* **Journal of Composites for Construction *24***: 04020011. DOI: https://doi.org/10.1061/(ASCE)CC.1943-5614.0001011.

[14] J. Korndörfer, B. Hoffmeister, and M. Feldmann. "Performance of steel columns subjected to vehicle impact–experimental and numerical studies". In: *5th ECCOMAS Thematic Conference on Computational Methods in Structural Dynamics and Earthquake Engineering*. 2015, 2926–2936.

[15] W. Li, Y.-Z. Gu, L.-H. Han, X.-L. Zhao, R. Wang, M. Nassirnia, and A. Heidarpour, (2019) *"Behaviour of ultra-high strength steel hollow tubes subjected to low velocity lateral impact: experiment and finite element analysis"* **Thin-Walled Structures *134***: 524–536. DOI: https://doi.org/10.1016/j.tws.2018.10.026.

[16] J. Fogarty and S. El-Tawil. "Collapse behavior of steel columns under lateral loading". In: *Structures Congress 2013: Bridging Your Passion with Your Profession*. 2013, 2848–2859. DOI: https://doi.org/10.1061/9780784412848.248.

[17] K. Kerileng, X. D. Zhi, and M. Dundu. "Response of duplex stainless steel circular hollow sections to lateral low-velocity impact loading". In: *Structures*. ***69***. Elsevier, 2024, 107442. DOI: https://doi.org/10.1016/j.istruc.2024.107442.

[18] K. Yang, X. Zhai, and H. Gao, (2025) *"Experimental and numerical studies on axial residual capacity of HSCHS tube after lateral impact"* **Thin-Walled Structures *215***: 113476. DOI: https://doi.org/10.1016/j.tws.2025.113476.

[19] X. Li, X. Zhu, R. Wang, T. Li, Y. Gu, and Q. Zhang, (2024) *"Experimental study on the impact resistance of hollow thin-walled aluminum alloy tubes and foam-filled aluminum tubes (6063-T5)"* **International Journal of Crashworthiness *29***: 95–114. DOI: https://doi.org/10.1080/13588265.2023.2183806.

[20] T. Zhang, Y. Wang, X. Zhai, X. Zhi, and Z. Cao, (2024) *"Finite element analysis of locally strengthened stainless-steel tube under lateral impact loading"* **Journal of Constructional Steel Research *218***: 108737. DOI: https://doi.org/10.1016/j.jcsr.2024.108737.

[21] S. Lipa and M. Kotełko, (2013) *"Lateral impact of tubular structure–theoretical and experimental analysis. Part 1–Investigation of single tube"* **Journal of theoretical and applied mechanics *51***: 873–882.

[22] N. R. Ravaliya and P. K. Gupta, (2024) *"Damage analysis and energy absorption capacity of hollow square steel tubes subjected to conical hammer impact"* **Australian Journal of Structural Engineering *25***: 34–54. DOI: https://doi.org/10.1080/13287982.2023.2242097.

[23] S. Dehghanpour, H. Khalili, S. A. F. A. R. I. K. E. Y. V. A. N. Hosseini, and Y. Mohammadi, (2015) *"Experimental and numerical investigation of lateral loading of thin-walled tube with different indenter"* **Journal of Simulation and Analysis of Novel Technologies in Mechanical Engineering *8***(3): 173–184.

[24] P. Heng, M. Hjiaj, J.-M. Battini, and A. Limam, (2016) *"A simplified model for nonlinear dynamic analysis of steel column subjected to impact"* **International Journal of Non-Linear Mechanics *86***: 37–54. DOI: https://doi.org/10.1016/j.ijnonlinmec.2016.07.005.

[25] Y. Chen, J. Wan, K. Wang, and S. Han, (2017) *"Residual axial bearing capacity of square steel tubes after lateral impact"* **Journal of Constructional Steel Research *137***: 325–341. DOI: https://doi.org/10.1016/j.jcsr.2017.06.019.

[26] S. Xiang, Y. He, and X. Zhou, (2021) *"Behaviour and failure modes of steel parking structure column under transverse impact"* **Thin-Walled Structures *167***: 108163. DOI: https://doi.org/10.1016/j.tws.2021.108163.

[27] K. Yokoya, (2019) *"Deformation Behavior of a Polygonal Tube under Oblique Impact Loading"* **Materials Research Proceedings *13***: DOI: https://doi.org/10.21741/9781644900338-7.

[28] J. George and N. NI, (2017) *"A Finite Element Study of Eccentricity in Axial Compression and Transverse Impact Loading on Cold Formed Stiffened Steel Column"* **Applied Mechanics and Materials** ***857***: 13–18. DOI: https://doi.org/10.4028/www.scientific.net/AMM.857.13.

[29] J. Fogarty, T. Y. Wu, and S. El-Tawil, (2017) *"Collapse response and design of deep steel columns subjected to lateral displacement"* **Journal of Structural Engineering** ***143***: 04017130. DOI: https://doi.org/10.1061/(ASCE)ST.1943-541X.0001848.

[30] M. Papadrakakis, V. Papadopoulos, and V. Plevris. "VALIDATION OF A NUMERICAL AND ANALYTICAL MODEL OF IMPACTED COLUMNS BY MEANS OF SMALL-SCALE DROP WEIGHT EXPERIMENTS". In: *5th ECCOMAS Thematic Conference on Computational Methods in Structural Dynamics and Earthquake Engineering*, 2937–2950.

[31] A.-Z. Zhu, W. Xu, K. Gao, H.-B. Ge, and J.-H. Zhu, (2018) *"Lateral impact response of rectangular hollow and partially concrete-filled steel tubular columns"* **Thin-Walled Structures** ***130***: 114–131. DOI: https://doi.org/10.1016/j.tws.2018.05.009.

[32] N. Abdel-Rahman and K. S. Sivakumaran, (1997) *"Material properties models for analysis of cold-formed steel members"* **Journal of Structural Engineering** ***123***: 1135–1143. DOI: https://doi.org/10.1061/(ASCE)0733-9445(1997)123:9(1135).

[33] Z. Tao, Z.-B. Wang, and Q. Yu, (2013) *"Finite element modelling of concrete-filled steel stub columns under axial compression"* **Journal of constructional steel research** ***89***: 121–131. DOI: https://doi.org/10.1016/j.jcsr.2013.07.001.

[34] G. R. Cowper and P. S. Symonds. *Strain-hardening and strain-rate effects in the impact loading of cantilever beams*. 1957. DOI: 10.21236/AD0144762.

[35] P. Baltay and A. Gjelsvik, (1990) *"Coefficient of friction for steel on concrete at high normal stress"* **Journal of Materials in Civil Engineering** ***2***: 46–49. DOI: https://doi.org/10.1061/(ASCE)0899-1561(1990)2:1(46).

[36] M. Zeinoddini, G. A. R. Parke, and J. E. Harding, (2002) *"Axially pre-loaded steel tubes subjected to lateral impacts: an experimental study"* **International Journal of Impact Engineering** ***27***: 669–690. DOI: https://doi.org/10.1016/S0734-743X(01)00157-9.